Electronic Supplementary Material (ESI) for Journal of Materials Chemistry A.
This journal is © The Royal Society of Chemistry 2018

Supporting Information

Nest-like V_3O_7 self-assembled by porous nanowires as anode supercapacitor material and its performance optimization through bonding with N-doped carbon

Danyang Zhao[1], Qiancheng Zhu[1], Dejian Chen, Xi Li, Ying Yu[b,*] and Xintang Huang[a,*]

Institute of Nanoscience and Nanotechnology, College of Physical Science and Technology, Central China Normal University, Wuhan 430079, China

∗ Corresponding author. [a] *E-mail: xthuang@mail.ccnu.edu.cn*

[b] *Email: yuying01@mail.ccnu.edu.cn*

1. The authors contributed equally to this work.

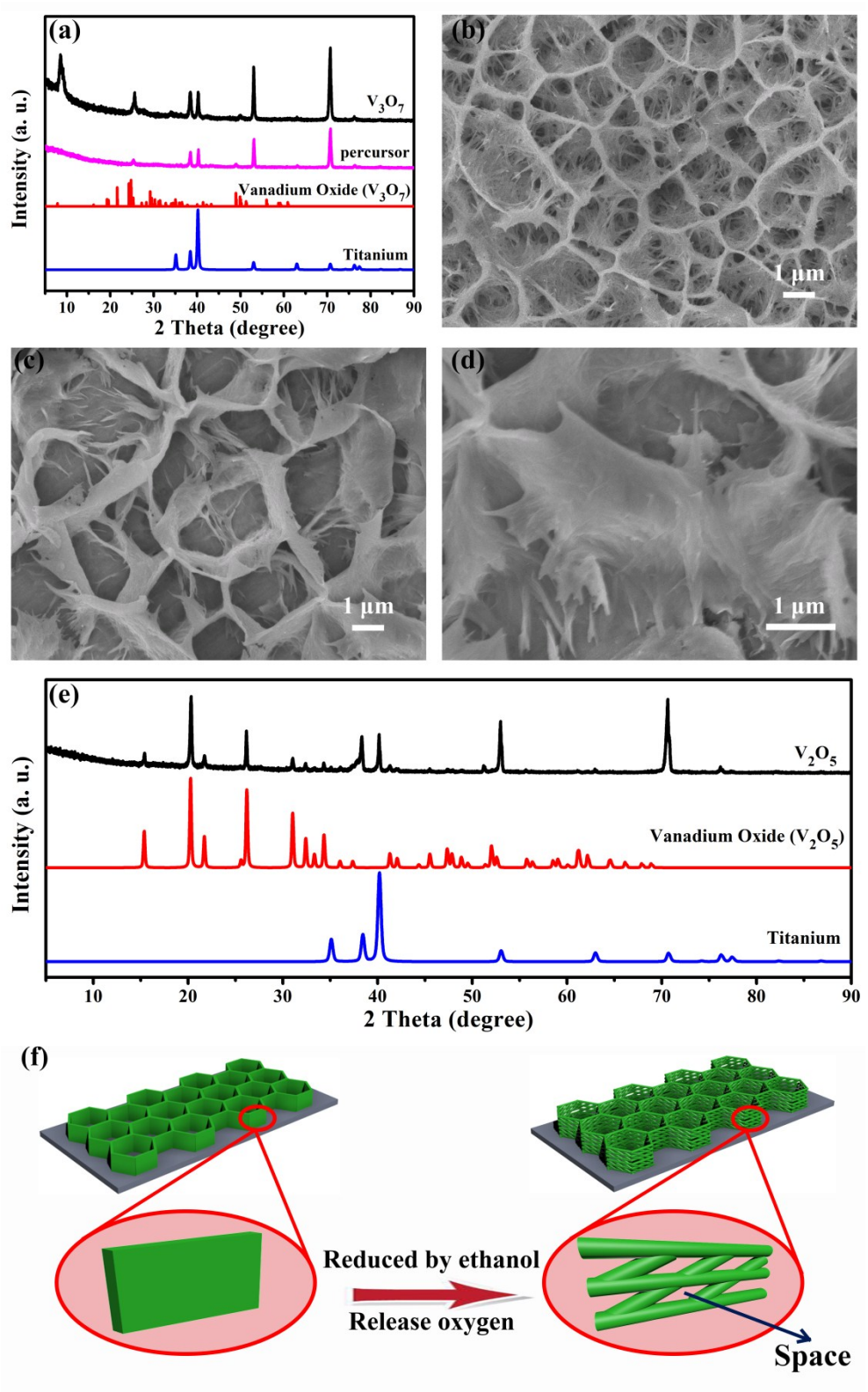

Figure S1. (a) XRD patterns of V_3O_7 and the precursor. (b) SEM image of the precursor. (c) and (d) SEM images of V_2O_5 without ethanol in hydrothermal process. (e) XRD patterns of V_2O_5 (JCPDS card no.9-387). (f) Evolution mechanism of the

nanowires of nest-like V_3O_7.

The phase composition and the nanostructure of the precursor after hydrothermal process is the same as the calcined V_3O_7 as shown in Figures S1a and S1b. To investigate the reason why the nest-like V_3O_7 was assemmbled by nanowires, the sample without ethanol was prepared. The SEM images in Figures S1c and S1d showed that the morphology was similar as nest-like V_3O_7. The difference is that the nanosheets were intact and smooth, but it was not assembled by nanowires. XRD patterns in Figure S1e indicate that the product was V_2O_5 if there was no ethanol during the hydrothermal process. Thus, it is sure that the nanowires originated from the release of oxygen for that ethanol reduced the V_2O_5 to V_3O_7 and thereafter left the space between the nanowires as illustrated in Figure S1f.

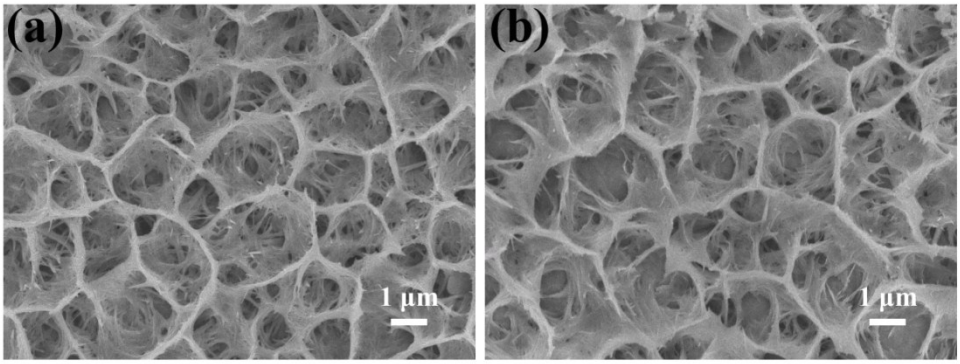

Figure S2. SEM images of (a) V_3O_7@PPy and (b) NC-V_3O_7.

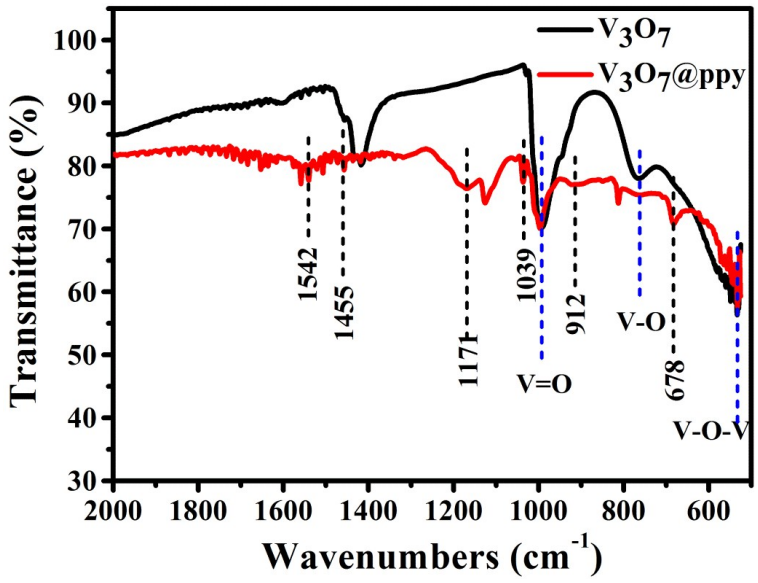

Figure S3. FT-IR spectra of V_3O_7 and V_3O_7@PPy.

The peaks of V_3O_7@PPy matched with those in the previous reports.[1, 2] The bands of V_3O_7 at 1000, 780 and 534 cm^{-1} were attributed to V=O, V-O and V-O-V vibration band, respectively. Those at 1542, 1455 and 1171 cm^{-1} were assigned to pyrrole ring and C–N stretching in PPy and the other peaks at 1039 and 678 cm^{-1} was resulted from the C–C stretching vibration and C–H out of plane bending of pyrrole moiety in PPy, respectively. Additionally, the one at 912 cm^{-1} indicated the doping state of PPy.

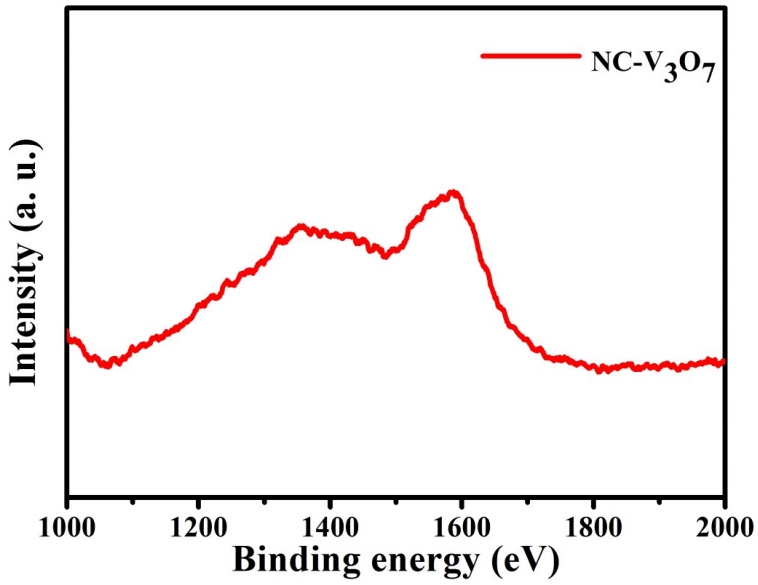

Figure S4. Raman spectrum of NC-V_3O_7.

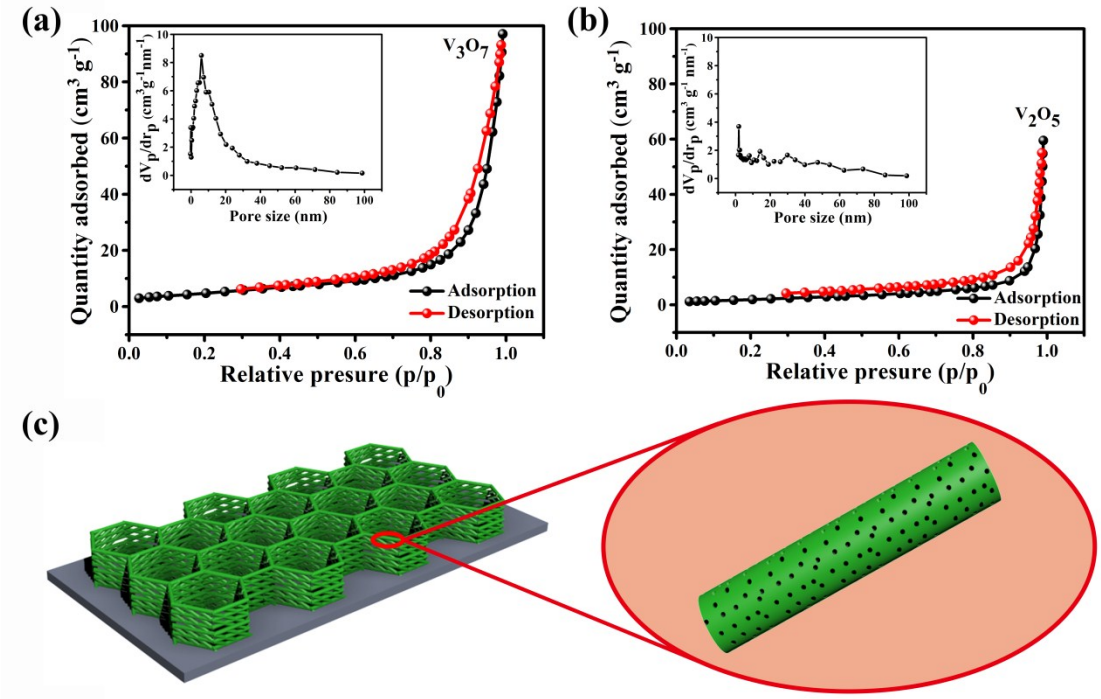

Figure S5. N_2 adsorption−desorption isotherm curves of V_3O_7 with ethanol (a) and V_2O_5 without ethanol (b) in hydrothermal process. (c) Schematic diagram of pores on V_3O_7 nanowires.

The pore distribution in Figures S5a (with ethanol) and S5b (without ethanol) exactly proves that the uniform pores originated from the reduction of V_2O_5 by ethanol in hydrothermal process. Till now, it is clear that the release of oxygen (ethanol reduced the V_2O_5 to V_3O_7) not only left the space to generate the nanowires (Figure S1f) but also produced the uniform pores as illustrated in Figure S5c.

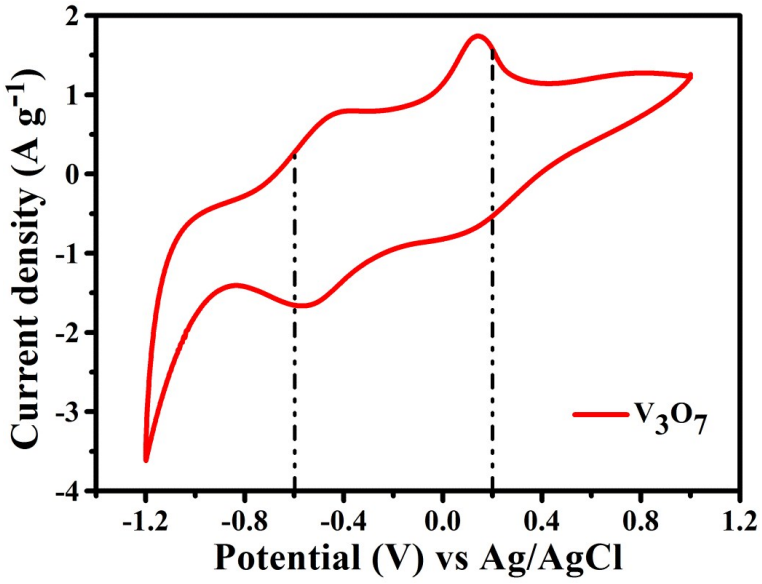

Figure S6. CV curve of V_3O_7 in potential window of -1.2 ~ 1 V at a current rate of 50 mV s^{-1}.

The CV test was performed at a scan rate of 50 mV s^{-1} between -1.2 ~1.2 V. It is found that the optimized potential range was -0.6 ~0.2 V marked by the dotted line for that the electrode was polarized beyond this range. The CV curve showed typical rectangular shape after corrected the potential range to -0.6 ~0.2 V as shown in Figure 3a.

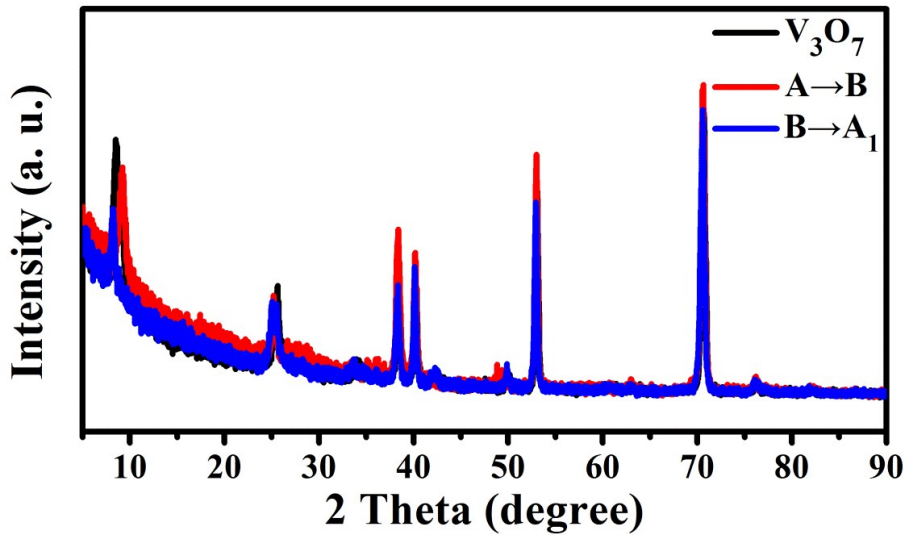

Figure S7. XRD pattern of V_3O_7 on three kinds of states.

Table.S1. Area percentage ratio of V^{4+} and V^{5+} of V_3O_7 at point A, B and A_1.

V at different valence states	**V^{4+}**	**V^{5+}**
initial potential of 0.2 V (point A)	30.66%	59.34%
lowest potential of -0.6 V (point B)	52.40%	47.7%
final potential 0.2 V (point A_1)	26.82%	73.18%

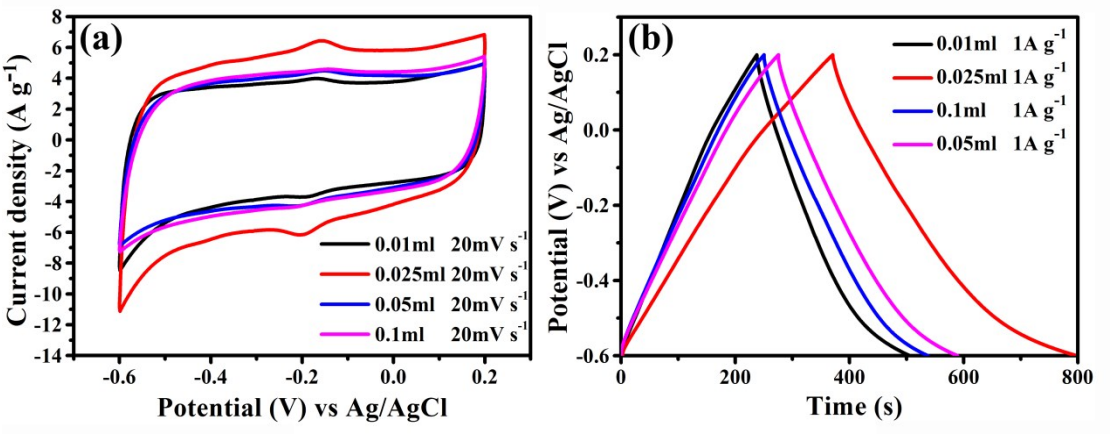

Figure S8. (a) CV and (b) GCD curves of NC-V_3O_7 with different N-doped carbon thickness through controlling the dosage of pyrrole monomer.

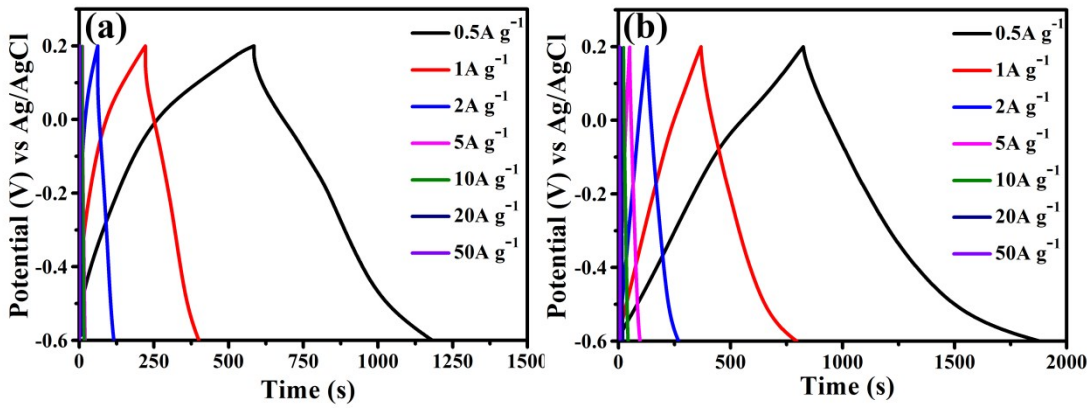

Figure S9. GCD curves of (a) V_3O_7 and (b) NC-V_3O_7 at various current densities.

Table S2. Comparison of our capacity with that of the recent published vanadium oxide and other anode materials (the references are shown in the main text).

Ref	**Material**	**Current density (A g^{-1})**	**Capacitance (F g^{-1})**
This work	NC-V_3O_7	0.5	660.63
Ref. 30	α-MoO_3 nanorod	0.1	214
Ref. 32	V_2O_3 nanoflakes@C core-shell composites	0.05	205
Ref. 33	graphene/VO_2 nanobelt composite hydrogel	1	191
Ref. 35	hierarchical vanadium oxide microspheres	0.6	456
Ref. 43	V_4O_9 microflowers	0.5	392
Ref. 44	Fe_3O_4@Carbon Nanosheets	0.5	586
Ref. 45	synthesize graphite- (Thiophene-2,5-diyl)-co-(benzylidene)	0.3	296

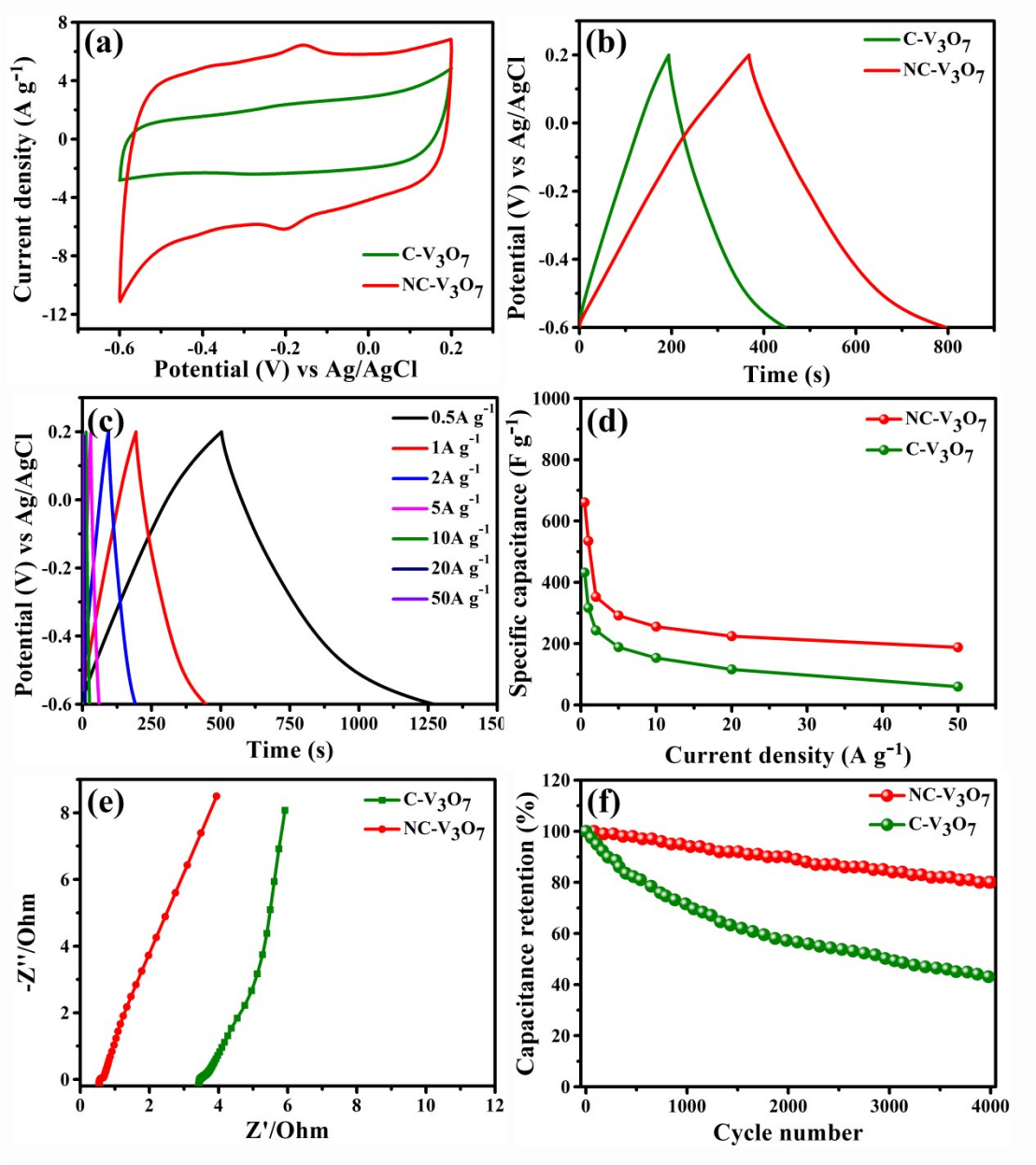

Figure S10. (a) CV curves of C-V_3O_7 and NC-V_3O_7 at a current rate of 20 mV s^{-1}; (b) GCD curves of C-V_3O_7 and NC-V_3O_7 at 1A g^{-1} from -0.6 to 0.2 V; (c) GCD curves for C-V_3O_7 at different scan rates; (d) rate capability of V_3O_7 and C-V_3O_7 calculated from the charge/discharge curves as a function of current density; (e) EIS spectra of V_3O_7 and C-V_3O_7; (f) cycle performance of C-V_3O_7 and NC-V_3O_7 at a current density of 10 A g^{-1}.

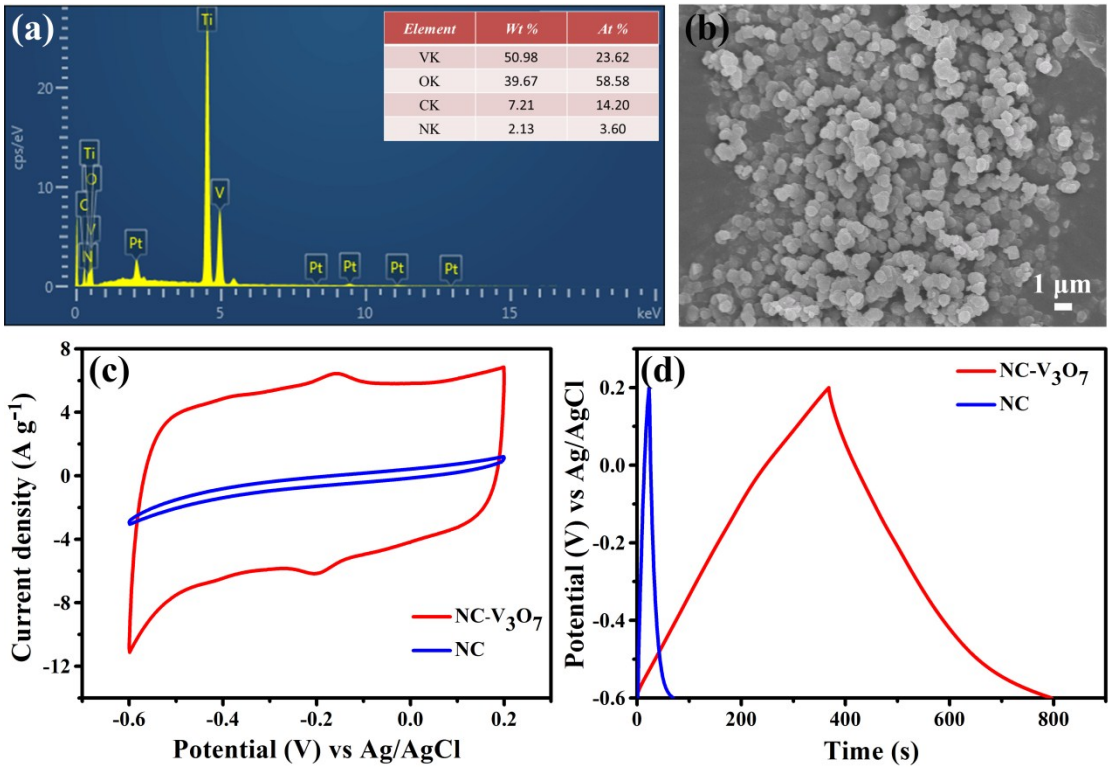

Figure S11. (a) EDS date of NC-V_3O_7. (b) SEM image of pure N-doped carbon. (c) CV curves of pure N-doped carbon (NC) and NC-V_3O_7 at a current rate of 20 mV s^{-1}. (d) GCD curves of NC and NC-V_3O_7 at 1A g^{-1} from -0.6 to 0.2 V.

The EDS results indicate that mass percent of C is only 7.21 % and N is only 2.13 %. Thus, the main composition in NC-V_3O_7 is V_3O_7. Pure N-doped carbon was fabricated with the same process as that for NC-V_3O_7. In a typical procedure, 30 ml ethanol solution was dropped into 1 ml pyrrole monomer to form a homogeneous mixture solution in a beaker. After that, pyrrole monomer was polymerized to PPy in-situ under UV light. Finally, the powder was calcined at 400 ℃ for 2 h in Ar to fabricate the pure N-doped carbon. The N-doped carbon particles were shown in Figure S11b. The capacitance of pure N-doped carbon was much lower than NC-V_3O_7 as shown in the CV curves (Figure S11c) and GCD curves (Figure S11d). Thus, the superior performance of NC-V_3O_7 is believed to the synergy of N-doped carbon and V_3O_7 and

the high capacitance of NC-V_3O_7 is derived from the V_3O_7 promoted by NC. N-doped carbon contributed very little capacitance for NC-V_3O_7.

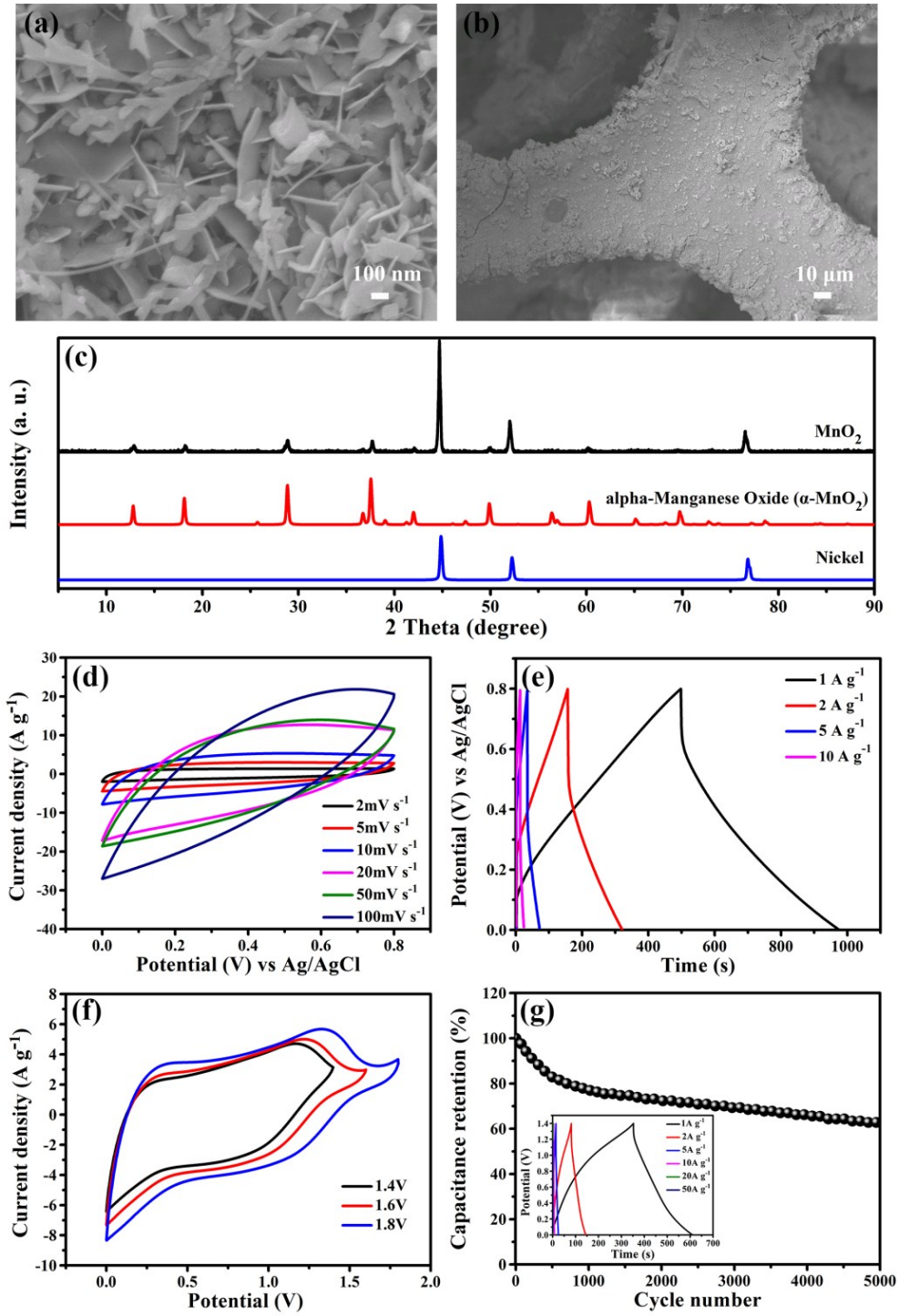

Figure S12. (a-b) SEM images of the cathode material MnO_2 nanosheets grown on Ni foam; (c) XRD patterns of MnO_2 on Ni foam; CV (d) and GCD (e) curves of MnO_2 at different scan rates; (f) CV curves collected in different potential windows of the assembled asymmetric supercapacitor; (g) cycling stability of the asymmetric device at

a current density of 10 A g^{-1}, the inset is GCD curves of device at different current density.

MnO_2 nanosheets were prepared through a hydrothermal method as we reported before.[1] The SEM images of MnO_2 nanosheets are shown in Figures S12a and S12b. XRD patterns indicates that the phase composition was α-MnO_2 (Figure S12c). The CV and GCD curves of MnO_2 are shown in Figures S12d and S12e, which indicates that MnO_2 is suitable using as a cathode material at the potential window of 0 ~ 0.8 V. The MnO_2//NC-V_3O_7 can be also operated at the voltage of 1.4 V without obvious polarization judged by the CV (Figure S12f) and GCD curves (the inset in Figure S12g). As shown in the main text in Figure 6d, the energy density of the asymmetric supercapcitor device (MnO_2//NC-V_3O_7) was higher than that of the symmetric device (NC-V_3O_7//NC-V_3O_7) at lower power density but the symmetric device was superior to the asymmetric device at higher power density. Additionally, the cycle performance of the symmetric device (Figure 6c) was also better than that of the asymmetric device (Figure S12g). To sum up, the symmetric device (NC-V_3O_7//NC-V_3O_7) is superior in stability and energy density especially at high power density, which can be due to the perfect matching of NC-V_3O_7//NC-V_3O_7, presumably, the two electrodes of NC-V_3O_7 in symmetric device have the same structure and chemical composition.

References:

1 Q. C. Zhu, K. Liu, J. Q. Zhou, H. Hu, W. J. Chen and Y. Yu, *Chem. Eng. J.*, 2017, **321**, 554.

2 Y. F. Zhang, X. H. Liu, D. Z. Chen, L. Y, J. R. Nie, S. P. Yi, H. B. Li and C. H, *J. Alloys Comp.*, 2011, **509**, L69.